

# Probing the active surface sites for CO reduction on oxide-derived copper electrocatalysts

Arнау Verdaguer-Casadevall,<sup>1‡</sup> Christina W. Li,<sup>2‡</sup> Tobias P. Johansson,<sup>1</sup> Soren B. Scott,<sup>1</sup> Joseph T. McKeown,<sup>3</sup> Mukul Kumar,<sup>4</sup> Ifan E. L. Stephens,<sup>1</sup> Matthew W. Kanan,<sup>2\*</sup> and Ib Chorkendorff<sup>1\*</sup>

<sup>1</sup> Center for Individual Nanoparticle Functionality, Department of Physics, Building 312, Technical University of Denmark (DTU), DK-2800, Kongens Lyngby, Denmark

<sup>2</sup> Department of Chemistry, Stanford University, 337 Campus Drive, Stanford, CA 94305, United States

<sup>3</sup> Materials Science Division, Lawrence Livermore National Laboratory, 7000 East Avenue, Livermore, CA 94550, United States

<sup>4</sup> Materials Engineering Division, Lawrence Livermore National Laboratory, 7000 East Avenue, Livermore, CA 94550, United States

## Supporting Information Placeholder

**ABSTRACT:** CO electroreduction activity on oxide-derived Cu (OD-Cu) was found to correlate with metastable surface features that bind CO strongly. OD-Cu electrodes prepared by H<sub>2</sub> reduction of Cu<sub>2</sub>O precursors reduce CO to acetate and ethanol with nearly 50 % Faradaic efficiency at moderate overpotential. Temperature programmed desorption of CO on OD-Cu revealed the presence of surface sites with strong CO binding that are distinct from the terraces and stepped sites found on polycrystalline Cu foil. After annealing at 350 °C, the specific current density for CO reduction is 44-fold lower and the Faradaic efficiency for ethanol and acetate is less than 5%. This loss of activity is accompanied by a reduction in the proportion of strong CO binding sites. We propose that the active sites for CO reduction on OD-Cu surfaces are strong CO binding sites that are supported by grain boundaries. Uncovering these sites is a first step towards understanding the surface chemistry necessary for efficient CO electroreduction.

The use of renewable energy to convert CO<sub>2</sub> into chemicals and fuels is an attractive means of mitigating emissions and increasing energy security.<sup>1,2</sup> Electrochemical CO<sub>2</sub> conversion could be pivotal to this goal; electrolyzers allow for fast startup and require little infrastructure, which would enable deployment of decentralized CO<sub>2</sub> recycling units scaled to local renewable energy sources. One strategy for efficient electrochemical CO<sub>2</sub> conversion is to separate the process into two steps: CO<sub>2</sub> reduction to CO, followed by CO reduction to oxygenates and hydrocarbons. Numerous CO<sub>2</sub> reduction catalysts have been reported that may enable practical CO<sub>2</sub> to CO conversion at low temperature.<sup>3-8</sup> Copper is the only catalyst that has shown significant CO reduction activity in aqueous electrolyte.<sup>9,10</sup> However, the overpotential required to drive CO reduction on bulk polycrystalline Cu is prohibitively high, which indicates that the low-index terrace and stepped facets that dominate the bulk Cu surface are inefficient catalysts. We recently showed that nanocrystalline Cu prepared via reduction of a Cu<sub>2</sub>O precursor, “oxide-derived Cu” (OD-Cu), has unprecedented activity for the reduction of CO to acetate, ethanol, and propanol.<sup>11</sup> Transmission electron microscopy (TEM) revealed that OD-Cu consists of an interconnected network of nanocrystallites with randomly-oriented grain boundaries at the crystallite interfaces. Dispersed nanoparticles of comparable dimensions did not

show enhanced CO reduction catalytic activity. Based on these data, we hypothesized that grain boundaries were responsible for creating the active sites for CO reduction. Insight into the surface chemistry of OD-Cu is vital for extracting design principles that may lead to improved catalysts.

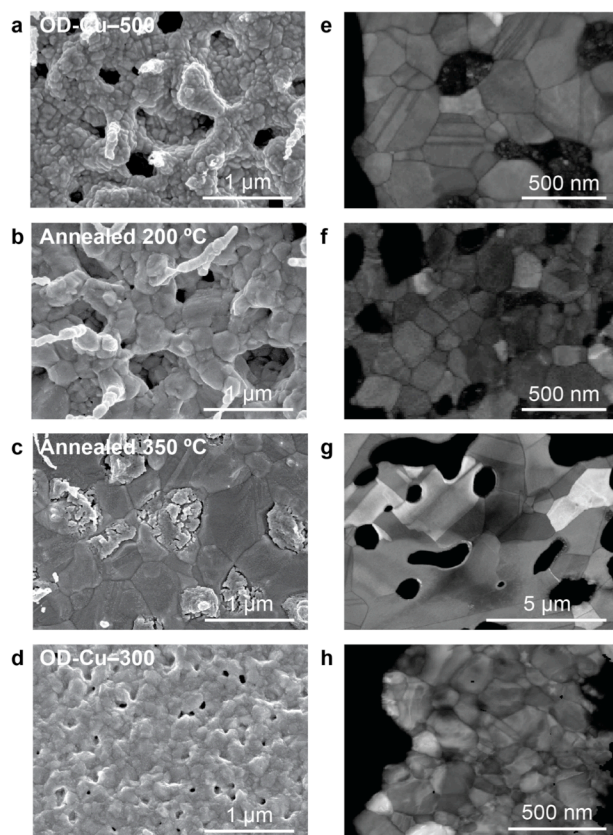


**Figure 1.** SEM (a-d), image quality (IQ) maps constructed from electron diffraction data (e-h) of oxide-derived Cu electrodes. (a, e) OD-Cu oxidized at 500 °C and reduced in H<sub>2</sub> (OD-Cu-500), (b, f) OD-Cu-500 after 200 °C anneal in N<sub>2</sub>, (c, g) after 350 °C anneal in N<sub>2</sub> (d, h) OD-Cu oxidized at 300 °C and reduced in H<sub>2</sub> (OD-Cu-300).

This study examines the impact of OD-Cu microstructure and adsorbate binding thermodynamics on electrocatalytic CO reduction activity. By comparing OD-Cu as-prepared to thermally annealed derivatives, we show that both the nanograined structure and CO reduction activity of OD-Cu are metastable. Temperature-programmed desorption (TPD) of CO is then used to probe the binding strength of CO on the surfaces of these electrodes.<sup>12</sup> We show that CO reduction activity correlates with the abundance of strong binding sites that are not found on terraces or stepped surfaces. TPD has been used to study high-temperature bulk catalysts such as Cu/ZnO/Al<sub>2</sub>O<sub>3</sub> for methanol synthesis<sup>12,13</sup> as well as model surfaces for low-temperature electrocatalysis,<sup>14-16</sup> but to the best of our knowledge this is the first time TPD has been used on active nanocrystalline electrocatalysts.

OD-Cu can be prepared by either electrochemical or H<sub>2</sub> reduction of Cu oxide precursors. For this study, H<sub>2</sub> reduction was used to facilitate TPD experiments. OD-Cu samples were synthesized via air oxidation at 500 °C followed by H<sub>2</sub> reduction at 130 °C (herein referred to as OD-Cu-500).<sup>11</sup> Scanning electron microscopy (SEM) showed aggregated particles in a porous morphology. Transmission electron microscopy nanodiffraction indicated that the material is composed of irregularly shaped, 100–300 nm grains that are joined by grain boundaries in a dense polycrystalline network (Fig. 1a, e). In order to modulate its structure and catalytic activity, OD-Cu-500 electrodes were annealed under N<sub>2</sub> at 200 °C and 350 °C. Annealing at 200 °C had little effect on the grain size, while annealing at 350 °C resulted in a smoother morphology and significantly increased grain sizes of ~1 μm (Fig. 1b, c, f, g). For comparison, an OD-Cu electrode was prepared by growing the oxide in air at 300 °C for 30 min and reducing in H<sub>2</sub> at 130 °C (OD-Cu-300). The grain sizes in OD-Cu-300 are similar to those of OD-Cu-500 and its 200 °C-annealed derivative, but OD-Cu-300 has a much smoother morphology (Fig 1d, h). Cross-sectional SEM revealed that OD-Cu-300 is essentially non-porous (Figure S6).

To further characterize the grain boundaries, orientation maps were collected on all OD-Cu samples. This TEM-based technique collects nanodiffraction patterns over scanned regions of a sam-

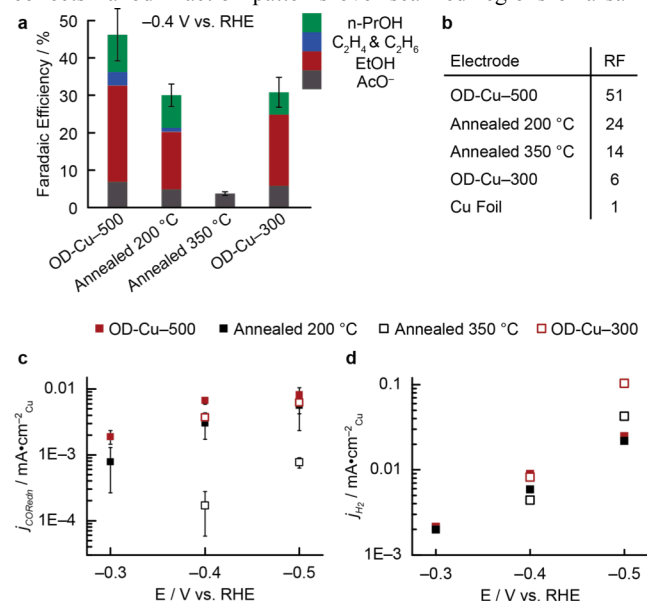


**Figure 2.** (a) Faradaic efficiency for CO reduction at -0.4 V vs. RHE in CO-saturated 0.1 M KOH. The remainder of the charge passed is H<sub>2</sub> evolution. (b) Electrochemical roughness factors (RF), measured from the capacitance in a non-Faradaic potential regime, with Cu foil defined as 1. (c) Specific current density for CO reduction vs. potential. (d) Specific current density for H<sub>2</sub> evolution vs. potential. The error bars represent one standard deviation from the mean based on 2–5 measurements.

ple, providing information for nanostructures analogous to that acquired using electron backscattering diffraction mapping in an SEM.<sup>17,18</sup> The nanodiffraction patterns are indexed to generate grain orientation and grain boundary maps from which grain boundary density and misorientation angles can be extracted. From this analysis, the grain boundary densities of OD-Cu-500, OD-Cu-500 annealed at 200 °C, and OD-Cu-300 are similar:  $15 \pm 2 \mu\text{m}^{-1}$ ,  $13 \pm 1 \mu\text{m}^{-1}$ , and  $21 \pm 2 \mu\text{m}^{-1}$ , respectively (Figure S9, S10, S11, S13). Moreover, the distribution of grain boundaries is similar in these three electrodes, with ~37% low-energy twin boundaries and the rest randomly oriented and non-twin coincident site lattice boundaries (Figure S9–S14). By contrast, the OD-Cu-500 electrode annealed at 350 °C has a much lower grain boundary density of  $1.7 \pm 0.1 \mu\text{m}^{-1}$  with ~53% low-energy twins (Figure S9, S12).

X-ray diffraction and X-ray photoelectron spectroscopy (XPS) of all four samples indicate that the only bulk crystalline phase present is Cu<sup>0</sup>, and the surface comprises primarily Cu<sup>0</sup> with some Cu<sup>1+</sup> due to native oxide formation during transfer of the sample to the XPS chamber (Figure S1–S4). The electrochemically active surface area of each sample was assessed using an electrochemical capacitance measurement. OD-Cu-500 has a roughness factor of 51 (where electropolished Cu foil is 1) arising from the high surface area porous structure. The roughness factor drops to 24 and 14 after annealing at 200 °C and 350 °C, respectively. OD-Cu-300 has a roughness factor of 6, lower than that of both thermally annealed electrodes.

Electrochemical activity for CO reduction was assessed over a range of potentials via constant potential electrolysis in 0.1 M KOH electrolyte, continuously purged with 1 atm of CO. The CO reduction activity of OD-Cu-500 has been previously reported.<sup>11</sup> OD-Cu-500 exhibits peak Faradaic efficiency of 48% for CO reduction at -0.4 V vs. RHE and generates C2 and C3 products including acetate, ethanol, n-propanol, ethylene, and ethane (Fig 2a), measured by gas chromatography and nuclear magnetic resonance (NMR). The surface-area normalized partial current density for CO reduction ( $j_{COredn}$ ) increases with increasing overpotential, but rapidly reaches a plateau corresponding to the mass-transport limit of ~1 mM dissolved CO in water (Fig 2c).<sup>19</sup>

Upon annealing, the intrinsic CO reduction activity of the electrode is significantly reduced. The surface-area corrected  $j_{COredn}$  is attenuated 2.5-fold on the 200 °C-annealed sample and 44-fold on the 350 °C-annealed sample relative to as-prepared OD-Cu-500 (Fig. 2c). The loss of intrinsic CO reduction activity is reflected in the Faradaic efficiencies for CO reduction at -0.4 V vs. RHE (Fig 2a). The ratios of oxygenate to hydrocarbon products remain similar, but there is a drop in total Faradaic efficiency for CO reduction and a corresponding increase in Faradaic efficiency for H<sub>2</sub> evolution. While the 200 °C-annealed sample still shows 30% total Faradaic efficiency for CO reduction, the 350 °C-annealed electrode has less than 5% efficiency, which is comparable to what was seen previously with commercial Cu nanoparticles. The loss of CO reduction activity upon annealing suggests that the catalytically active sites are tied to metastable structural features that are kinetically trapped during the low-temperature H<sub>2</sub> reduction of the Cu<sub>2</sub>O precursor. In contrast, annealing has little effect on the surface area-corrected partial current density for H<sub>2</sub> evolution ( $j_{H2}$ ) (Fig 2d).

The catalytic activity of OD-Cu depends on the thickness of the Cu<sub>2</sub>O precursor. OD-Cu-300 is prepared from a thinner oxide and is intrinsically less active for CO reduction than OD-Cu-500. In fact, OD-Cu-300 has essentially the same surface area-corrected  $j_{COredn}$  and CO reduction Faradaic efficiency as OD-Cu-500 after annealing at 200 °C. Since OD-Cu-300 has 4-fold lower roughness factor than the 200 °C annealed electrode, this result indicates that neither electrode porosity nor microscopic surface area

are significant determinants of CO reduction catalytic activity. This conclusion is further supported by the comparison between OD-Cu-500 annealed at 350 °C and OD-Cu-300. OD-Cu-300 has lower surface area but much higher CO reduction activity than the 350 °C annealed sample.

In order to connect catalytic activity to the thermodynamics of adsorbate binding on the surface, CO-TPD was used to probe the surface chemistry of OD-Cu. To prepare OD-Cu samples for TPD, Cu foil was oxidized externally and mounted in the UHV chamber. Adventitious contamination from exposure to air was removed by mildly sputtering the surface and the samples were subsequently reduced at 130 °C under a flow of 1 bar of H<sub>2</sub> (see the Supporting Information). XPS at this stage showed a metallic Cu surface (Fig. S17) with no trace of nickel (a common contaminant in UHV in the presence of CO due to the formation of nickel carbonyl in the gas lines<sup>20</sup>) or other metallic impurities. The samples were cooled down to 77 K, and CO was dosed into the chamber. The temperature was then ramped up at 2 K s<sup>-1</sup> and a mass spectrometer monitored the signal from CO at mass 28. The annealed OD-Cu-500 samples were prepared in an identical manner to OD-Cu-500 and annealed in UHV at 200 °C or 350 °C prior to CO dosing. The experiments were carried out with a constant dosage of 200 L, which results in variable CO coverage given the different surface areas of the samples (Fig. S15).

Figure 3a shows a typical TPD profile for electropolished polycrystalline Cu foil. Based on literature data from single crystalline Cu,<sup>12,21,22</sup> the TPD features can be assigned to different facet terminations. The lowest temperature desorption feature, from 100 K to 200 K, is due to low index facets such as Cu(111) and Cu(100), which bind CO weakly. The higher temperature feature between 200 K and 250 K is characteristic of stepped sites such as Cu(211). Figure 3b shows the CO-TPD profile of OD-Cu-500. The OD-Cu-500 profile shows a high-temperature feature centered at 275 K that is clearly absent from the profiles for polycrystalline Cu and single crystalline Cu but is present in different proportions in the profiles for the other OD-Cu samples (Fig. 3b-e, —). Annealing OD-Cu-500 to 200 °C and 350 °C reduces the area of the high-temperature feature (Figures 3c-d). The profile of OD-Cu-300 exhibits broader and less-defined peaks than OD-Cu-500 and its annealed derivatives because its low roughness factor results in a higher CO coverage. Nonetheless, the high-temperature feature is clearly still present on OD-Cu-300 (Fig. 3e).

Two possible factors could account for the high-temperature feature in the OD-Cu profiles: (i) CO readsorption in the catalyst layer, which causes peak broadening and a shift of the peak maximum to higher temperature or (ii) surface sites with enhanced binding to CO. Both of these effects have been observed in TPD studies on industrial Cu/ZnO/Al<sub>2</sub>O<sub>3</sub> and Cu/SiO<sub>2</sub> catalysts.<sup>23,24</sup> OD-Cu-500 has a large roughness factor and a significant fraction of the sample surface may reside in mesopores where readsorption could occur. However, OD-Cu-300 has a roughness factor of only 6, which is the lowest of the OD-Cu samples and 2.5-fold lower than the 350 °C-annealed sample. Despite its lower roughness factor, OD-Cu-300 presents a higher proportion of the high-temperature feature than the 350 °C annealed sample, indicating that readsorption alone cannot account for the high-temperature feature on OD-Cu.

Direct, quantitative interpretation of the TPD profiles shown here is not possible because the roughness factor and morphology of each sample is different. The same CO dosage gives variations in surface coverage and differing degrees of readsorption on each sample, both of which affect the relative proportions of the low-index, stepped, and strong-binding TPD features. To decouple these effects, the TPD profiles of polycrystalline Cu and the OD-Cu samples were simulated using microkinetic modeling of CO

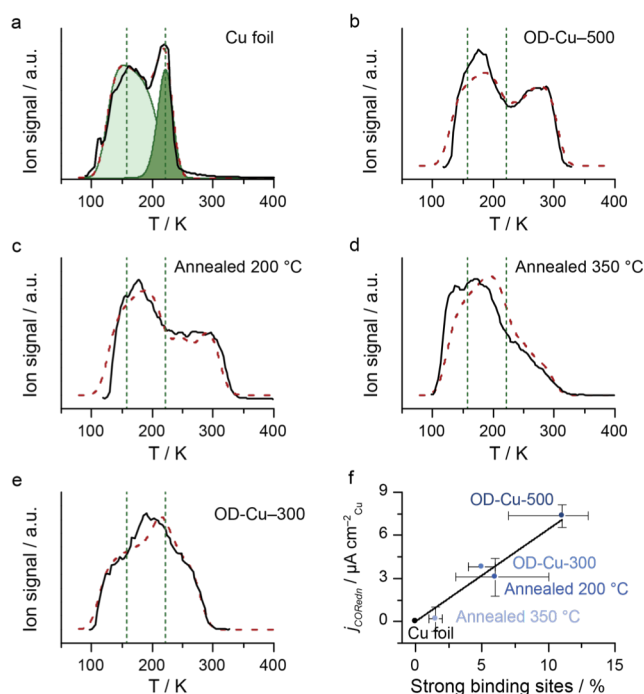


**Figure 3.** TPD profiles for various Cu samples. a-e) Experimental data (solid black lines) and resulting fit from microkinetic simulations (dashed red lines). The dotted green lines indicate the central position of the low-index facets and stepped sites in polycrystalline Cu. a) Polycrystalline Cu. Features arising from low-index facets are highlighted in light green, undercoordinated sites are highlighted in dark green; b) OD-Cu-500; c) OD-Cu annealed at 200 °C; d) OD-Cu annealed at 350 °C; e) OD-Cu-300; f) overlay of TPD profiles. Measurements were performed at a ramp rate of 2 K s<sup>-1</sup> with a CO dose of 200 L. g) Experimental CO reduction activity at -0.4 V as a function of the percentage of strong binding sites, estimated from simulations of the TPD profiles. The solid black line is a linear fit through all points. The error bars are a means of showing uncertainty in the simulations and have been obtained by varying pore depth in the model by ±5 μm or 50 %, whichever is lowest.

binding to Cu surfaces with different binding sites and porosities (Fig. 3a-e, ---).

To determine the contribution of readsorption to the OD-Cu profiles, simulations were performed for porous polycrystalline Cu with two binding sites that have adsorption energies of ~52 and ~60 kJ/mol, which correspond to low-index and stepped facets of Cu (described in the Supporting Information). As shown in Figure S21, increasing the depth of the porous layer causes a shift of the TPD profile to higher temperature. While simulated porous polycrystalline Cu has a major peak at 260 K, the overall profile clearly does not fit that of OD-Cu. It is only possible to model the experimental TPD profile for OD-Cu by including a strong binding site with adsorption energy of ~67 kJ/mol.

The microkinetic model also enabled quantification of the relative proportions of each surface site on OD-Cu. OD-Cu-500 has the largest proportion of strong-binding sites with 11% surface coverage. The proportion drops to 5% after annealing at 200 °C and 1.5% after annealing at 350 °C. While these percentages have large uncertainty due to assumptions made about the electrode pore structure, the proportion of strong-binding sites is clearly reduced by thermal annealing. The proportion of strong-binding sites on OD-Cu-300 is 5%. When plotted against electrochemical activity, a linear correlation is obtained between surface area-corrected  $j_{\text{COredn}}$  and the percentage of strong binding sites at the electrode surface (Fig 3f). On the basis of this correlation, we propose that the active sites for CO reduction at low overpotential on Cu are strong-binding sites. Strong CO binding may increase

the rate of CO reduction at a surface site by increasing its steady-state CO coverage. In addition, a high density of strong binding sites at a surface region created by a bulk defect may be necessary if the rate-limiting step involves reductive CO coupling.<sup>25,26</sup> However, these strong-binding sites may not be sufficient for CO reduction. The OD-Cu-500 electrode annealed at 350 °C retains 1.5% of the strong binding site despite having  $j_{\text{CORedn}}$  that is 4-fold lower than that of polycrystalline Cu foil, which has only terrace and step sites (Figure S8, Table S4). The broad high-temperature feature observed in TPD does not reflect a single surface atomic structure; rather it most likely consists of a range of strained or defective structures, all of which bind CO more strongly within a ~10 kJ/mol range. As such, it is possible that only a small subset of these defective structures is capable of catalyzing the CO reduction reaction. In addition, CO is simply a probe molecule in these experiments. In electrolyte solution with an applied potential, the relevant catalytic transition state structures and binding energies may not scale with the CO binding energy in UHV.

Grain boundaries are bulk phenomena, but they can affect the surface of the sample probed in TPD experiments. The reduction in the proportion of strong binding sites upon thermal annealing qualitatively correlates to the microstructural change observed in TEM. The 7-fold drop in strong binding sites percentage is similar to the 9-fold drop in grain boundary density observed between OD-Cu-500 and the electrode after 350 °C annealing. Notably, the proportion of strong binding sites estimated by microkinetic modeling of the TPD profiles is significantly larger than the proportion of the surface corresponding to grain boundary surface terminations. Based on the grain boundary orientation maps and assuming a 1 nm boundary width, we estimate that OD-Cu-500 has 1-2% coverage of grain boundary surface termination area while the TPD modeling indicates 7-15% coverage of strong binding sites. If the grain boundaries are responsible for creating all of the strong binding sites, these results indicate that the surface terminations affect the structure and binding properties of a region that encompasses a much larger width of 4-10 nm. Previous simulations of nanocrystalline fcc metals have shown that grain boundaries strain the surfaces up to several nm away<sup>27</sup>. Annealing of the samples up to a certain temperature would leave grain boundaries unaffected, but relax out metastable strong binding sites.

In summary, we present evidence that the high CO reduction activity on OD-Cu is correlated to surface sites that bind CO more strongly than low-index and stepped Cu facets. These metastable sites may arise from the disordered surfaces at grain boundary and defect terminations, which are stabilized by the interconnected nanocrystalline network. Further structural and mechanistic elucidation of the surface chemistry of OD-Cu, in particular regarding the exact nature of the active site, will enable the design and synthesis of more efficient catalytic materials for CO reduction.

## ASSOCIATED CONTENT

### Supporting Information

Experimental procedures and additional data. This material is available free of charge via the Internet at <http://pubs.acs.org>.

## AUTHOR INFORMATION

### Corresponding Authors

\*mkanan@stanford.edu, ibchork@fysik.dtu.dk

### Author Contributions

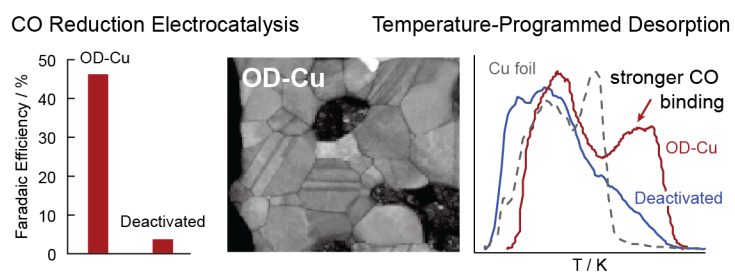
‡These authors contributed equally to this work.

## ACKNOWLEDGMENT

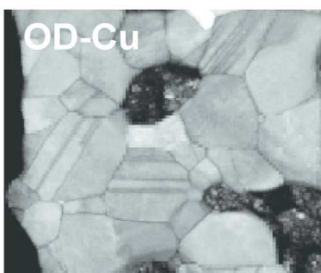
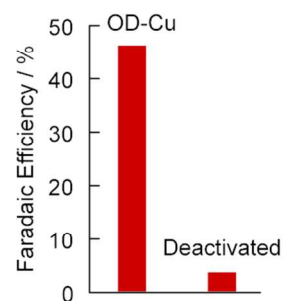
The Danish National Research Foundation's Center for Individual Nanoparticle Functionality is supported by the Danish National Research Foundation (DNRF54). We thank the Global Climate and Energy Project (106765) and the AFOSR (FA9550-14-1-0132). C.W.L. gratefully acknowledges a Stanford Graduate Fellowship. Sample characterization was performed at the Stanford Nano Shared Facilities. Lawrence Livermore National Laboratory is under the auspices of the U.S. Department of Energy, Contract No. DE-AC52-07NA27344. J. T. M. and M. K. were supported by the Office of Basic Energy Sciences, Division of Materials Science and Engineering under FWP #SCW0939.

## REFERENCES

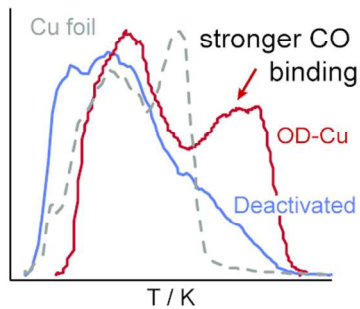
- (1) Hori, Y. In *Modern Aspects of Electrochemistry*; Vayenas, C. G., White, R. E., Gamboa-Aldeco, M. E., Ed.; Springer: New York, 2008; Vol. 42, p 89.
- (2) Appel, A. M.; Bercaw, J. E.; Bocarsly, A. B.; Dobbek, H.; DuBois, D. L.; Dupuis, M.; Ferry, J. G.; Fujita, E.; Hille, R.; Kenis, P. J. A.; Kerfeld, C. A.; Morris, R. H.; Peden, C. H. F.; Portis, A. R.; Ragsdale, S. W.; Rauchfuss, T. B.; Reek, J. N. H.; Seefeldt, L. C.; Thauer, R. K.; Waldrop, G. L. *Chem Rev* **2013**, *113*, 6621.
- (3) Chen, Y. H.; Li, C. W.; Kanan, M. W. *J Am Chem Soc* **2012**, *134*, 19969.
- (4) DiMeglio, J. L.; Rosenthal, J. *J Am Chem Soc* **2013**, *135*, 8798.
- (5) Zhu, W. L.; Michalsky, R.; Metin, O.; Lv, H. F.; Guo, S. J.; Wright, C. J.; Sun, X. L.; Peterson, A. A.; Sun, S. H. *J Am Chem Soc* **2013**, *135*, 16833.
- (6) Mistry, H.; Reske, R.; Zeng, Z. H.; Zhao, Z. J.; Greeley, J.; Strasser, P.; Cuenya, B. R. *J Am Chem Soc* **2014**, *136*, 16473.
- (7) Lu, Q.; Rosen, J.; Zhou, Y.; Hutchings, G. S.; Kimmel, Y. C.; Chen, J. G.; Jiao, F. *Nat Commun* **2014**, *5*.
- (8) Asadi, M.; Kumar, B.; Behranginia, A.; Rosen, B. A.; Baskin, A.; Reppin, N.; Pisasale, D.; Phillips, P.; Zhu, W.; Haasch, R.; Klie, R. F.; Kral, P.; Abiade, J.; Salehi-Khojin, A. *Nat Commun* **2014**, *5*, 4470.
- (9) Hori, Y.; Takahashi, R.; Yoshinami, Y.; Murata, A. *J Phys Chem B* **1997**, *101*, 7075.
- (10) Schouten, K. J. P.; Qin, Z. S.; Gallent, E. P.; Koper, M. T. M. *J Am Chem Soc* **2012**, *134*, 9864.
- (11) Li, C. W.; Ciston, J.; Kanan, M. W. *Nature* **2014**, *508*, 504.
- (12) Fu, S. S.; Somorjai, G. A. *Surf Sci* **1992**, *262*, 68.
- (13) Sandoval, M. J.; Bell, A. T. *J Catal* **1993**, *144*, 227.
- (14) Perez-Alonso, F. J.; McCarthy, D. N.; Nierhoff, A.; Hernandez-Fernandez, P.; Strebel, C.; Stephens, I. E. L.; Nielsen, J. H.; Chorkendorff, I. *Angew Chem Int Edit* **2012**, *51*, 4641.
- (15) van der Niet, M. J. T. C.; den Dunnen, A.; Jurlink, L. B. F.; Koper, M. T. M. *Angew Chem Int Edit* **2010**, *49*, 6572.
- (16) Johansson, T. P.; Ulrikkeholm, E. T.; Hernandez-Fernandez, P.; Escudero-Escribano, M.; Malacrida, P.; Stephens, I. E. L.; Chorkendorff, I. *Phys Chem Chem Phys* **2014**, *16*, 13718.
- (17) LaGrange, T.; Reed, B. W.; Wall, M.; Mason, J.; Barbee, T.; Kumar, M. *Appl Phys Lett* **2013**, *102*.
- (18) Rauch, E. F.; Veron, M.; Portillo, J.; Bultreys, D.; Maniette, Y.; Nicolopoulos, S.; 2008, S5. *Microscopy and Analysis* **2008**, *22*, S5.
- (19) In *IUPAC Solubility Data Series*; Cargill, R. W., Ed.; Pergamon Press: Oxford, 1990; Vol. 43.
- (20) Nerlov, J.; Sckerl, S.; Wambach, J.; Chorkendorff, I. *Appl Catal A-Gen* **2000**, *191*, 97.
- (21) Vollmer, S.; Witte, G.; Woll, C. *Catal Lett* **2001**, *77*, 97.
- (22) Makino, T.; Okada, M. *Surf Sci* **2014**, *628*, 36.
- (23) Strunk, J.; d'Alnoncourt, R. N.; Bergmann, M.; Litvinov, S.; Xia, X.; Hinrichsen, O.; Muhler, M. *Phys Chem Chem Phys* **2006**, *8*, 1556.
- (24) d'Alnoncourt, R. N.; Bergmann, M.; Strunk, J.; Löffler, E.; Hinrichsen, O.; Muhler, M. *Thermochim Acta* **2005**, *434*, 132.
- (25) Montoya, J. H.; Shi, C.; Chan, K.; Nørskov, J. K. *J. Phys. Chem. Lett.* **2015**, *6*, 2032.
- (26) Calle-Vallejo, F.; Koper, M. T. M. *Angew Chem Int Ed* **2013**, *52*, 7282.
- (27) Stukowski, A.; Markmann, J.; Weissmüller, J.; Albe, K. *Acta Mater* **2009**, *57*, 1648.



## CO Reduction Electrocatalysis



## Temperature-Programmed Desorption



95x34mm (300 x 300 DPI)